Subscriber access provided by Indiana University Libraries - Bloomington

Article

Studies of Nanoparticle-Assisted Photoannealing of Polydimethylsiloxane by Time-harmonic Photothermal Microscopy

Maryam Zahedian, Zachary Lee, Eun Sohl Koh, and Bogdan Dragnea

ACS Photonics, **Just Accepted Manuscript** • DOI: 10.1021/acsphotonics.0c00968 • Publication Date (Web): 06 Aug 2020

Downloaded from pubs.acs.org on August 20, 2020

Just Accepted

“Just Accepted” manuscripts have been peer-reviewed and accepted for publication. They are posted online prior to technical editing, formatting for publication and author proofing. The American Chemical Society provides “Just Accepted” as a service to the research community to expedite the dissemination of scientific material as soon as possible after acceptance. “Just Accepted” manuscripts appear in full in PDF format accompanied by an HTML abstract. “Just Accepted” manuscripts have been fully peer reviewed, but should not be considered the official version of record. They are citable by the Digital Object Identifier (DOI®). “Just Accepted” is an optional service offered to authors. Therefore, the “Just Accepted” Web site may not include all articles that will be published in the journal. After a manuscript is technically edited and formatted, it will be removed from the “Just Accepted” Web site and published as an ASAP article. Note that technical editing may introduce minor changes to the manuscript text and/or graphics which could affect content, and all legal disclaimers and ethical guidelines that apply to the journal pertain. ACS cannot be held responsible for errors or consequences arising from the use of information contained in these “Just Accepted” manuscripts.

is published by the American Chemical Society. 1155 Sixteenth Street N.W., Washington, DC 20036

Published by American Chemical Society. Copyright © American Chemical Society. However, no copyright claim is made to original U.S. Government works, or works produced by employees of any Commonwealth realm Crown government in the course of their duties.

Studies of Nanoparticle-Assisted Photoannealing of Polydimethylsiloxane by Time-harmonic Photothermal Microscopy

Maryam Zahedian, Zachary Lee, Eun Sohl Koh, Bogdan Dragnea*

Chemistry Department, Indiana University, Bloomington, Indiana 47405, USA

E-mail: dragnea@indiana.edu

Abstract

In nanoparticle-assisted photothermal microscopy, absorption of radiation by a nanoparticle is followed by non-radiative relaxation which leads to changes in the surrounding medium temperature, pressure, and density. Under harmonically modulated irradiation, the finite heat diffusion rate causes a phase delay between the thermal oscillation at a location in the medium relative to that at the nanoparticle surface. The phase delay averaged over the probe laser volume can be measured concomitantly with the amplitude of detected probe power modulation. In this study we show that, in conjunction with the more widespread measurement of the modulation amplitude, the photothermal phase can provide a complementary, sensitive probe of thermally-induced changes in the local medium properties. As proof of principle, we study a widely used, technologically important polymer resist – polydimethylsiloxane (PDMS). In addition we show how, with the help of simulations, it is possible to extract from phase/amplitude data the temperature-dependent properties of the photoannealed medium.

---

*To whom correspondence should be addressed

Keywords

photothermal, nanoparticles, heat diffusion, thermal curing, photoannealing

Due to their size-dependent, tunable optical properties, plasmonic nanoparticles (NPs) have been developed in the past few decades into sensors and heat nanosources for various applications, from cancer therapy[1–3] to new bolometers.[4] To control the effects of local heating, it is important to have a tool for nanoscale monitoring of the thermally-induced modifications triggered by individual plasmonic agents.[3,5] The ability of photothermal (PT) microspectroscopic imaging to detect and track NPs in non-absorbing media with nanometer resolution,[6,7] combined with measurement capabilities of the spectral absorption cross-section of single nanoscale features in a transparent medium,[8–10] make this method particularly appealing for studies of heat dissipation at nanoscale.

In the most common implementation of PT microscopy, heat dissipation effects in the medium caused by absorption of modulated light by the NP, are measured by phase-sensitive detection of changes in the propagation of a non-resonant probe beam.[11] The sequence of processes involved in generation of optical contrast is the following: After NP excitation, return to the ground state occurs via radiation or nonradiatively – by thermal relaxation. The latter induces an increase in the local temperature, which in turn produces transient changes in pressure and density of the embedding medium. When the photothermally-induced temperature change occurs faster than the time required for the medium to expand (or contract), the rapid pressure change can trigger an acoustic wave.[12] At longer times, a density change is expected due to the local temperature increase, which leads to an index of refraction change. The latter can be detected with high sensitivity by optical interferometric methods.[13,14] It is convenient to employ a time-harmonic modulated pump beam since the time-dependent portion of the detected signal can then be demodulated with high sensitivity by lock-in detection.[15,16]

The magnitude of the detected power at the modulation frequency is proportional to the wavelength-dependent absorption cross-section – a feature that allows performing absorption spectroscopic measurements free of scattering artifacts.[17–19]

The phase delay of the signal relative to the heating beam modulation, averaged over the focal probe volume, is a second parameter that can be simultaneously measured. The spatially-averaged phase delay contains information on the thermal transport characteristics of the medium, surrounding the particle. The realization that measuring heat transport dynamics can yield information about the local physical characteristics of the embedding medium elicited significant interest and already a number of studies have demonstrated it experimentally or theoretically. Heber *et al* have shown that the thermal diffusivity of an homogeneous medium can be extracted from experimental data by comparison to electromagnetic scattering calculations of the photothermal signal.[20,21] Großer *et al* have modeled particles at surfaces[22] and the specifics of nanoparticle heating by ultrafast laser pulses were discussed by Baffou and Rigneault.[23] Moreover, Pavlovetc *et al* have added chemical specificity and improved spatial resolution thus significantly extending the applicability of photothermal microscopy in materials studies.[24]

As a result of the local temperature increase, physical or chemical transformations of the medium surrounding the absorbing NP may occur.[25–27] Due to the fast local temperature transients and sharp local temperature gradients at nanoscale, far from equilibrum processes sometimes make for previously unknown phase behavior. For instance, nanoparticle heating in water leads to nanobubble formation. Depending on laser and solvent characteristics this non-equilibrium phase change may occur above the spinodal decomposition temperature of water at $\approx 320\ ^{\circ}C$[28] or at substantially lower (but still above the thermodynamic boiling point) temperatures.[29] In other works the bubble nucleation temperature appears to depend on solution parameters such as the amount of dissolved gas.[30] This effect has found applications in the optically-controlled injection of gold NPs into living cells.[31] Due to the strong optical scattering that ensues, plasmonic nanobubble dynamics could be characterized in detail, in real-time.[32–34] The improved mechanistic understanding and possibility of control of plasmonic nanobubble generation have made them promising candidates as localized active manipulation elements for high throughput microfluidic applications. However, despite the high technological interest, beyond nanobubble phenomena other local non-equilibrium transformations such as solid-solid or solid-liquid have not been studied in detail. Here, we show how simultaneously computing PT amplitude and phase and comparing the results with the experimental data can lead to the quantitative identification of such local transformations and, specifically, to the temperature-dependent properties of the photoannealed material.

The NP-embedding medium employed in this work is PDMS – a polymer widely used for the fabrication and prototyping of microfluidic chips.[35–37] PDMS is generally prepared from a base elastomer and a curing agent. Heat ($100 - 200\ ^{\circ}C$, for tens of minutes) is often applied after mixing to expedite cross-linking. This feature makes PDMS interesting for PT microscopy because of its intrinsic reliance on a local heat source, which is provided by the method. Thus, the degree of cross-linking could be supplemented if the medium has not been fully cured by the bulk treatment step. In this report we show that this is indeed the case. We also observe that, as cross-linking occurs in the vicinity of the PDMS-embedded NP under laser irradiation, the thermal properties of the medium change irreversibly. Our aim was to measure such changes and model them via a combination of thermal diffusion and optical scattering calculations. As a result of this approach, we provide estimates of the temperature-dependent thermal parameters of fully-crosslinked PDMS. We note that the PDMS medium utilized here for proof-of-principle experiments has been studied in conjunction with NPs in the context of attempts at improving PDMS thermal conductivity by addition of conductive NPs to lower the effect of hotspots generated in PDMS microchips.[14,38–41] Our results bear direct relevance to such studies.

Results and Discussion

In experiments, ligand-stabilized gold NPs of 44 nm diameter (see "Gold NP Synthesis" section) were distributed at the interface between two stacked PDMS layers forming $\sim$ 100 μm thick film supported on a silica glass microscope slide (see "Immobilizing Gold NPs in PDMS" section for details). Completely surrounding the NPs by PDMS simplifies modeling with respect to substrate-supported NPs since a substrate can add experimental uncertainties about the nature of the interface and complicate thermal and optical scattering computations.[20] Moreover, since PDMS has a lower thermal conductivity compared to glass, see Table 1, the PT detection limit is lower with respect to the case of NPs immobilized on a glass substrate.[20,42]

Table 1: Room-temperature thermal parameters of the PDMS, water, and glass and their melting or degradation points.[43–45]

Medium	κ $[W/m/K]$	Melting/Degradation point $[°C]$
PDMS	0.15	$500 - 600$ (degradation)
Water	0.61	0 (melting), 100 (boiling)
Glass	1.4	> 1000 (glass transition)

Experiments in PDMS

A schematic of the home-built PT apparatus is provided in Figure SI-1. Typical experiments start by raster-scanning a plane in the sample orthogonal to the optical axis (Oz) and simultaneously acquiring the modulation amplitude and phase of the detected power. PT signal amplitude and phase-shift are displayed as 2D (x-y) maps in Figure 1 (a-b). From histograms of single-particle PT detected power and phase we obtain the average signal amplitude and phase values used henceforth in this report, Figure 1 (c-d).

Since NPs are distributed at the interface between two stacked PDMS films (see the "Immobilizing Gold NPs in PDMS" Section) contributions from out-of-focus NPs are negligible and the spread can be considered planar.

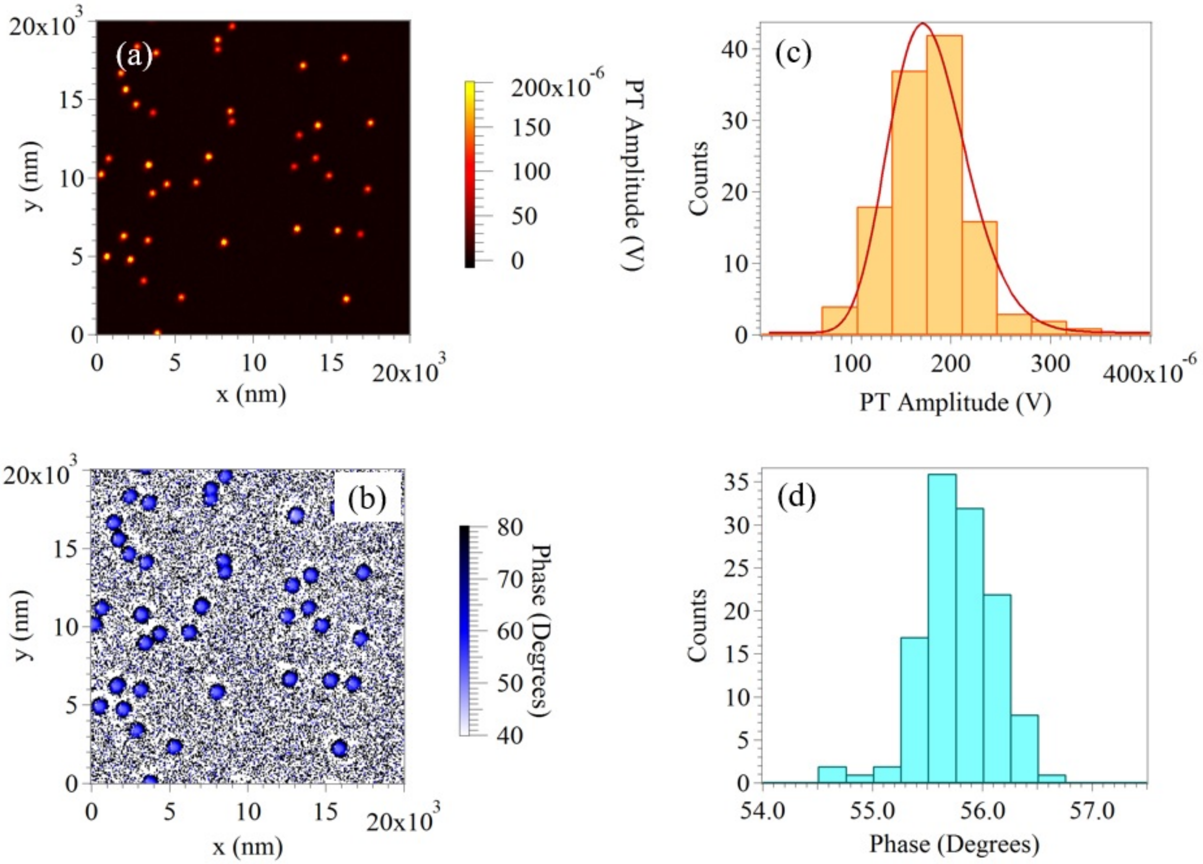

Figure 1: (a) Maps of PT amplitude and (b) phase from raster scanning a planar distribution of Au NPs with average diameter of $\sim$ 44 nm, at 150 μW heating laser power and 0.5 MHz modulation frequency. (c-d) Histograms of PT signal amplitude and phase corresponding to the NPs in (a-b).

Because of the finite thermal diffusivity of the medium, both the PT amplitude and phase are dependent on the frequency of heat modulation.[20] Figure SI-1 shows experimental data from a single NP illustrating how increasing the modulation frequency leads to an increase in the phase shift, and a decrease of the PT amplitude, consistent with previous work.[20] To maximize sensitivity to the dynamics of thermal diffusion without sacrificing the amplitude detection limit, in this work we have chosen the corner frequency of 0.5 MHz for pump modulation.

Figure 2 presents higher magnification x-y and x-z maps of amplitude and phase shift values for a single, representative NP. While the PT amplitude is maximum at the center and decays away from the peak value, the PT phase-shift line profiles exhibit a minimum at the center and increases with the distance from the NP center. The magnitude of this change is $\sim 3.5 - 12$ degrees, similar to previous work.[46] The increase in phase shift as the probe moves away from the concentric location is consistent with the retardation in the local temperature modulation due to the finite thermal diffusion velocity.

Note that in a coaxial heating-probe arrangement, the detected signal shows a zero-crossing when both the heating and the probe focal planes contain the center of the thermal lens. It follows that photothermal contrast can only be obtained in under-focusing or over-focusing conditions, which manifests itself as a two-lobe structure in x-z maps.[13] In this work, a slight focus mismatch of the pump and probe Δz_f has been chosen to make the magnitude of the first lobe (associated with under-focusing), larger than the second one. Measurements were always performed with the apparatus tuned on the maximum of the first lobe, i.e. in under-focusing conditions.

To observe both PT phase and amplitude as a function of heating power we have found convenient to plot amplitude *vs* phase with the heating power as a parameter, Figure 3. Maximum temperatures have been estimated from calculations using thermal constants for PDMS.[43]

To observe potential irreversible changes in the medium thermal properties, the heating power was swept up, down, and up again. Three heating regimes were observed. At low pump powers, (< 2.5 mW, $T_{max} \lesssim 250\ ^{\circ}C$), the PT phase gradually increases with amplitude, and the process is reversible, *i.e.* the phase–amplitude traces overlap, Figure 3 (a).

If we continue to increase the heating power in the range $2.5-4$ mW ($T_{max} \lesssim 400\ ^{\circ}C$) and decrease it back, the power–decrease trace does not overlap anymore with the first power–increase trace (Figure 3 (b)). However, when the power is increased again to the same limit as during the first increase, this second time the amplitude–phase trace does overlap with the first power–decrease trace (Figure 3 (c)). Such reversibility will continue to be observed with the condition, the experiment is repeated over the same heating power range. However, if the power is increased beyond the previous limit, the first (ramp-up) trace and the second

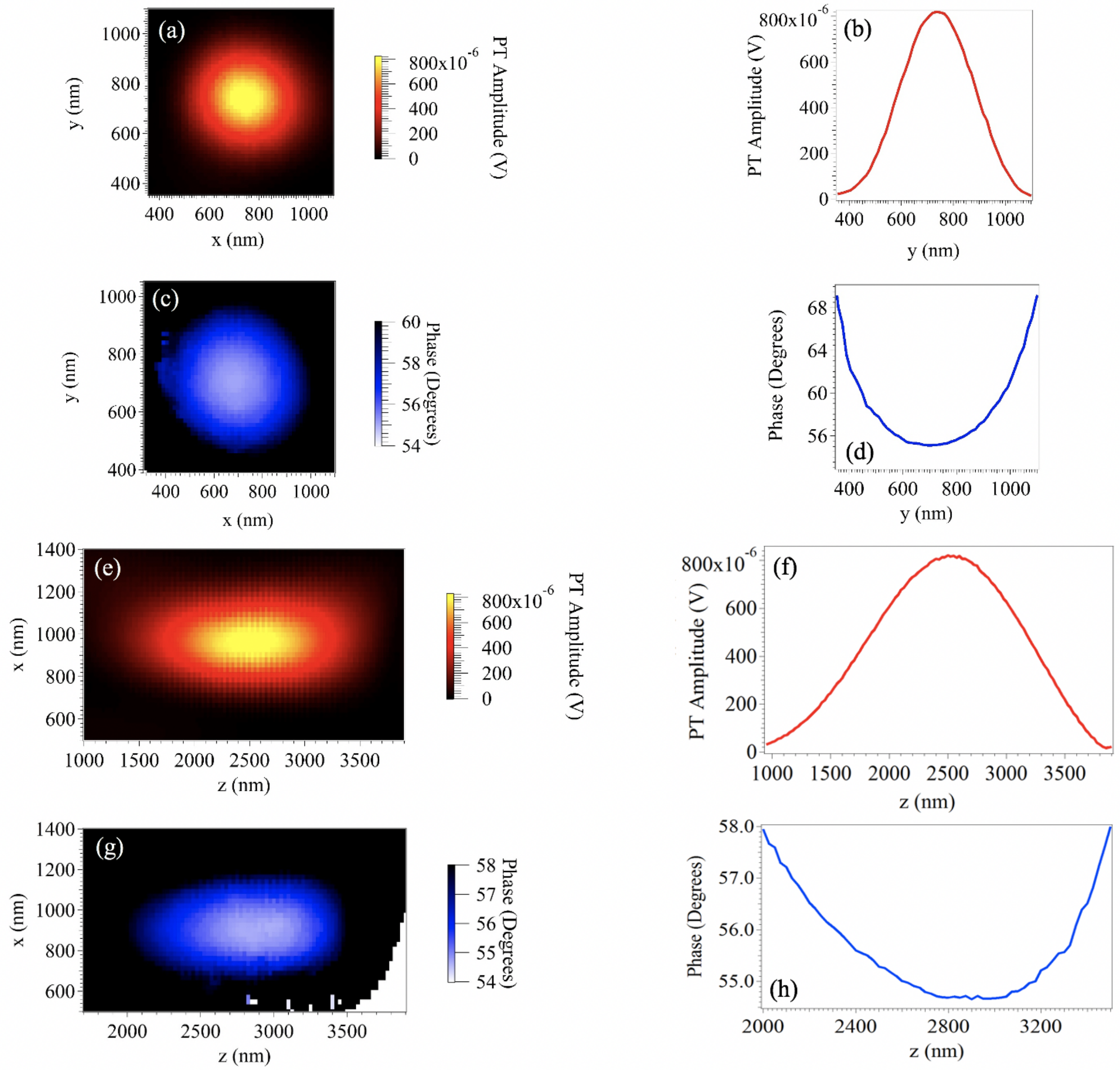

Figure 2: x-y and x-z maps and line profiles of PT amplitude and phase-shift for a single Au NP. (a) x-y PT amplitude map. (b) Line profile along the x-axis of (a). (c) PT phase x-y map. (d) Line profile along the x-axis in (c). (e) x-z PT amplitude map. (f) Line profile along z axis. (g) x-z PT phase map. (h) Line profile along z axis in (g). (All data at 1.5 mW heating power).

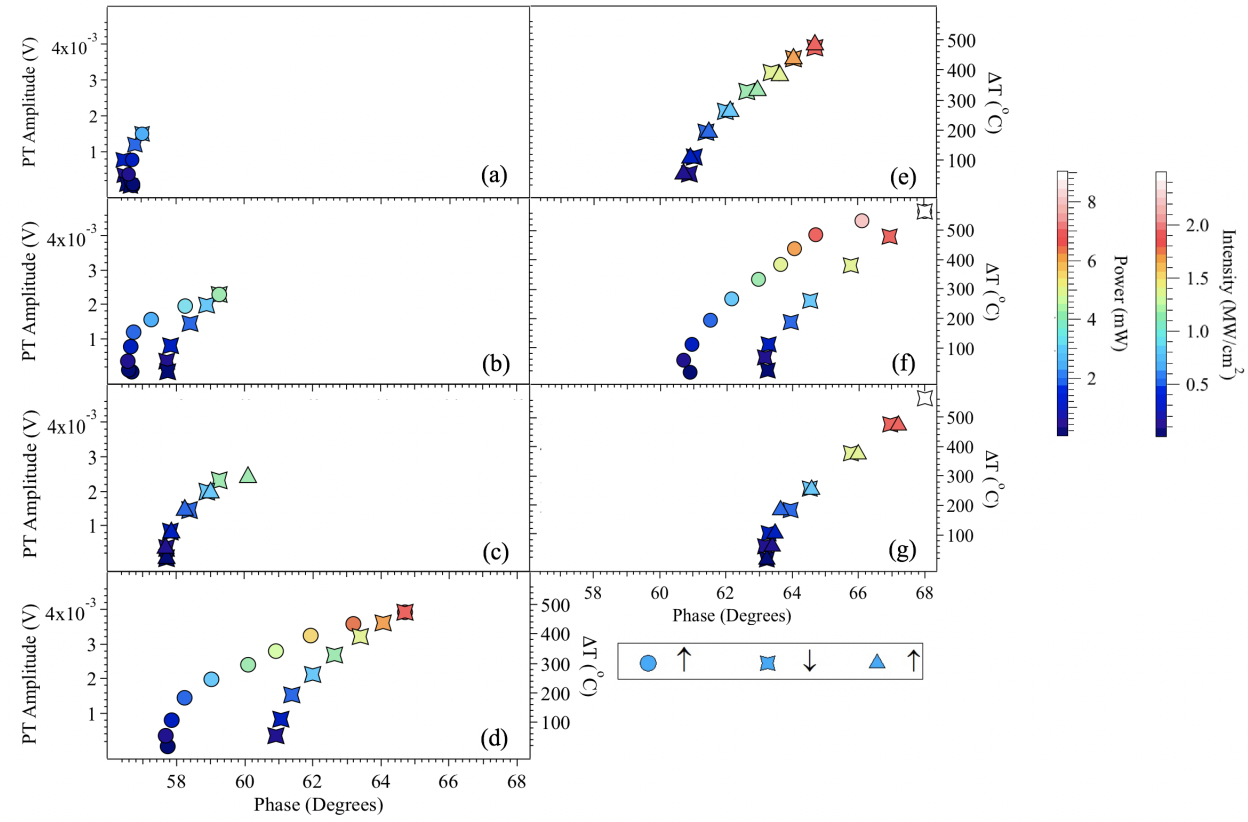

Figure 3: PT amplitude versus phase for pump powers 0.05-9 mW (45 nm Au NP). ↑ shows the heating power increase, and ↓ the heating power decrease. Maximum power (intensity) (a) 2.5 mW (0.69 MW/cm^2), (b) and (c) 4.0 mW (1.1 MW/cm^2), (d) and (e) 7.0 mW (1.93 MW/cm^2) , (f) and (g) 9.0 mW (2.48 MW/cm^2). Error bars are smaller than the symbols (values are provided in the experimental apparatus section, in the SI).

(ramp-down) trace do not overlap. This trend persists at higher pump powers, up to ≈ 9 mW (Figure 3 (d), (e), (f), and (g)).

Beyond ≈ 9 mW, the trend in the amplitude–phase ceases to be monotonical – the amplitude stays flat and even starts to decrease when heating power increases. Reversibility is not regained after the first sweep, like before. Since the estimated temperatures exceed those at which PDMS and even NP degradation might occur, we have not studied this regime in detail.

We are now turning our attention back to the second regime. The first time a particle is irradiated, the amplitude–phase curve is different from the subsequent ones which are all identical, provided the power sweep range is kept constant. This is consistent with a permanent material change that occurs at the first sweep, over a region where the temperature exceeds a certain value. For our PDMS preparation, that temperature appears to be between $\approx 200 - 300\ ^{\circ}C$. It is worth noting that, while the above behavior is easy to observe on amplitude–phase graphs, it is much less so when the amplitude is plotted against heating power, Figure 4. In this more common representation, it is easy to miss the material changes observed in the amplitude-phase diagram (Figure 3) because the amplitude *vs* heating power curves are almost overlapping. Therefore, there is a clear qualitative benefit to be gained from including phase in PT microscopy observations when the surrounding material is likely to undergo transformations.

Radial temperature profiles and estimates of the extent of a circular area where the maximum temperature is greater than a given threshold value (of $\approx 340\ ^{\circ}C$) are provided in Figure 5. As one may expect, the radius of this circular area varies as the square-root of the heating power (Figure 5(b)). Because of the $1/r$ dependence of temperature on the radial location, most of the PT signal originates within a shell several tens of nm thick.

It appears therefore that detectable irreversible modifications occur in the NP medium when heating power exceeds ≈ 3 mW. These changes presumably affect the PDMS thermal properties. They manifest particularly as shifts in the phase angle between the pump and

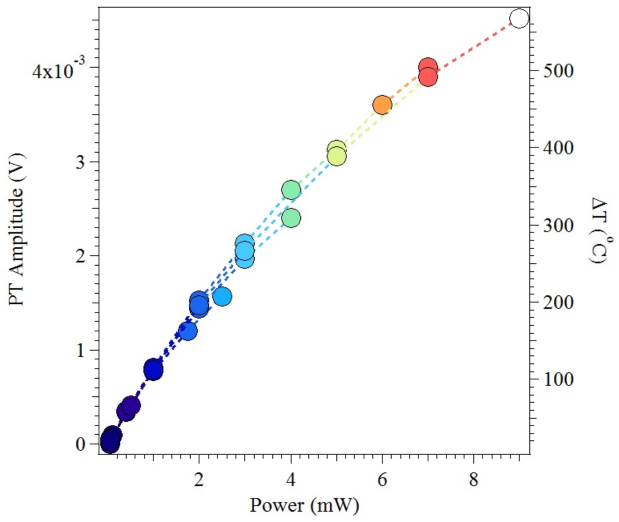

Figure 4: PT amplitude versus pump power (45 nm Au NP in PDMS).

the PT signal waveforms. This behavior is consistent with the existence of a threshold temperature for the transformation process, at $\approx 200-300\ ^{\circ}C$, which might correspond to a thermal activation barrier separating a different phase from the conventionally cured phase. Interestingly, Roberts *et. al.* have shown that local photocuring of epoxy resin using plasmonic NPs can create a stronger bond between composite materials than conventional thermal curing.[47]

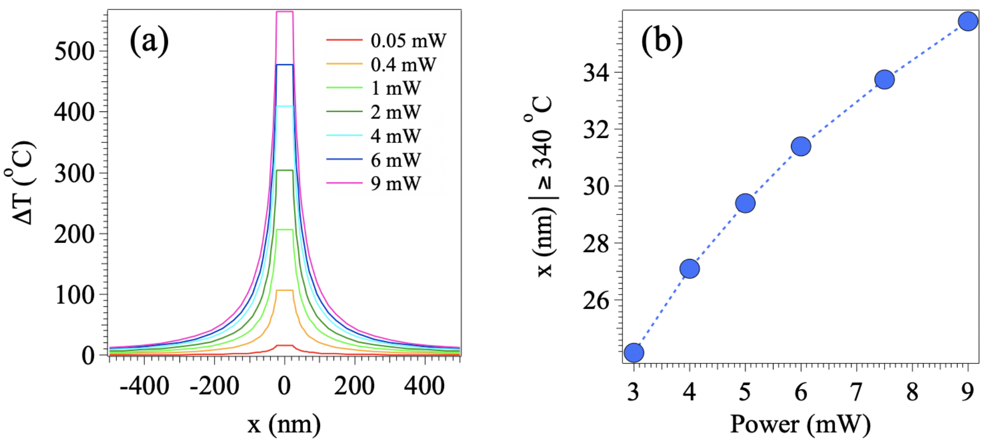

Figure 5: (a) Calculated temperature line profile along the x axis with heating power as parameter. (b) Calculated radius of a circular area with $\Delta T > 340\ ^{\circ}C$ as a function of heating power (45 nm Au NP in PDMS).

Experiments in Water

It is instructive to compare the PDMS behavior with that of water, a homogeneous substance whose thermal properties are well-understood.[44,48,49] Heber *et al.* have measured the PT response of free diffusing NPs in water.[20] Signal bursts were analyzed in both amplitude and phase, and the average thermal diffusivity for $\Delta T \sim 50\ ^{\circ}C$ was estimated with the aid of simulations.[20] Another way to study the photothermal properties would be to trap the NP.[8] Ideally, one would want to conduct the experiment in a homogeneous medium, free of substrate effects, similar to PDMS. However, because both amplitude and phase are sensitive to the positioning of the NP with respect to the probe focus, it would be challenging to hold the particle sufficiently steady in a fluid. Thus, we chose to do the experiment on NPs immobilized on a glass substrate (see "Binding of Gold NPs to the Glass Substrate" section for details). The calculated direct contact area with the substrate being less than 4 nm^2 for a 45 nm diameter NP, thermal diffusion in the vicinity of the NP was predominantly determined by the (water) medium (Table 1). Note, however, that for this experiment NP-substrate bonding had to be ensured in order to achieve stability against thermal desorption (see the "Binding of Gold NPs to the Glass Substrate" section).

Figure 6 (a) presents amplitude-phase data for estimated maximum temperatures of up to $\sim 140\ ^{\circ}C$. Signal amplitudes in water are much smaller than in PDMS. This is the result of $\sim 4\times$ faster cooling rate in water than in PDMS, Table 1. Second, the slope of the amplitude-phase curves is negative for water (while positive in PDMS). In other words, the phase shift in water decreases as the temperature increases. This is because in water above $20\ ^{\circ}C$ thermal diffusivity increases relatively rapidly with temperature. As discussed above, we expect a decrease in the phase shift when that happens. On the other hand, experiments on curable epoxy resins have shown that the glass-transition temperature increases with degree of curing. The result is a drop in the heat capacity at high temperatures, and of thermal diffusivity, for such polymers.[50] Therefore, heat propagation from the center of the probe volume to its boundary slows down as the temperature increases which results in a phase shift increase.

It is not unreasonable to expect PDMS to have similar thermal properties dependence on curing. Thus, PDMS and water exhibit opposite slopes in amplitude-phase diagrams due to opposite trends in their thermal parameter variations as a function of temperature.

As expected, the phase-amplitude diagram in Figure 6 (a) indicates a reversible heating process. We note that the maximum NP surface temperature ($\sim 140\ ^{\circ}C$) exceeds the thermodynamic bulk boiling temperature. However, formation of a bubble is not detected, presumably because the temperature is not high enough to drive the bubble growth against the kinetic barrier imposed by the Gibbs-Thompson effect. Nevertheless, ramping the power to reach a surface temperature above ($\sim 140\ ^{\circ}C$) leads to a jump in the phase shift for the power-down trace. Note that this difference between the power-up and power-down traces for water mostly has the phase-amplitude curves shifted horizontally by an equal amount without noticeable shape differences. This suggests that the phenomenon at the origin of the shift must be of a different nature from that responsible for the phase-amplitude curve changes in Figure 3 where the local slope is different between power-up and power-down curves. While the source of irreversibility for the water-glass medium remains unclear, it might concern changes in interfacial conductivity since NPs are ligand-stabilized,[46] which could influence heat conduction in the vicinity of the NP. A number of phenomena could be responsible for the latter such as explosive boiling with local substrate damage,[29,34,51] and even NP surface destabilization at higher heating powers.[52]

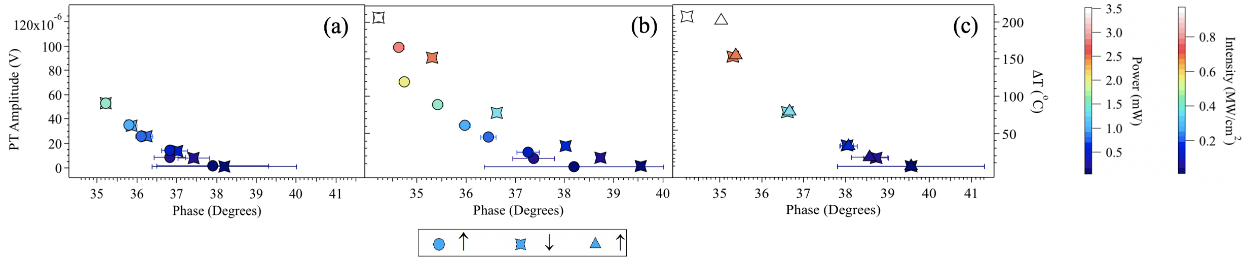

Figure 6: PT amplitude and maximum temperature estimates *vs.* pump power of 45 nm Au NP in water on a glass substrate (heating power 0.05-6.5 mW and 0.5 MHz modulation frequency. ↑ and ↓ indicate heating power increase and heating power decrease, respectively. Maximum power (intensity) (a) 1.5 mW ($0.4\ MW/cm^2$), (b) and (c) 3.5 mW ($1\ MW/cm^2$).

So far the results strongly suggest that the newly created shell has different properties than the initial, conventionally-cured PDMS. The change may include thermal as well as optical properties. To learn more about this modified material, we combine optical scattering simulations with time harmonic heat diffusion calculations to extract the local thermodynamic parameters in the vicinity of light absorbing NPs.

Estimating the Change in the Thermal Parameters of the Proximity shell upon NP-assisted Annealing of PDMS

To compare the calculated photodetected thermal power with the experiment, we have first computed the time-harmonic radial temperature distribution, which was then converted into an index of refraction time-harmonic radial distribution that served as the input for the optical scattering simulation. This computational approach was validated through comparisons with previously published work[20] (see Supporting Information, section on "Simulation Formalism" and "Simulations vs. Experiment in Water"). There is good agreement between simulations of Au NPs in water and experiment (Figure SI-8).

We now turn our attention to PDMS. When we assume a homogeneous medium surrounding the NP and having normal PDMS thermal parameters, simulations lead to a much faster slope in the PT magnitude *vs* heating power than the one observed experimentally from pre-annealed samples. Again, this supports the idea of an inhomogeneous medium that involves a new PDMS phase surrounding the NP. The possible origins of this departure can be rationalized as follows: In the quasi-static regime, i.e. for modulation frequencies less than 2 MHz, the amplitude of the PT detected power modulation is inversely proportional with the medium thermal conductivity, and proportional to the probe intensity. Inhomogeneities in the static index of refraction could affect the latter. For the moment we ignore this possibility, and assume that the departure from computational predictions is mainly due to a change in thermal conductivity. When the surrounding, modified shell thickness is comparable to the NP radius, Figure 5, the dominant PT signal contribution will originate within the shell. Thus, to simplify transient PT calculations, we assume a homogeneous surrounding medium with same parameters as the modified shell material. Figure 7 shows the experimentally detected PT power as a function of the heating power compared with simulations obtained at different thermal conductivities of the medium, starting at the normal value for PDMS. At low heating powers ($\sim$ 2 mW), experiment and computations agree. At higher powers the experimental trend better follows simulation curves that correspond to thermal conductivities approximately $4-6\times$ higher than the normal value for PDMS. We note that an increase in thermal conductivity could be expected if the medium becomes denser (higher sound velocity) or more homogeneous (longer phonon mean free path length),[53,54] which are both reasonable outcomes of the annealing.

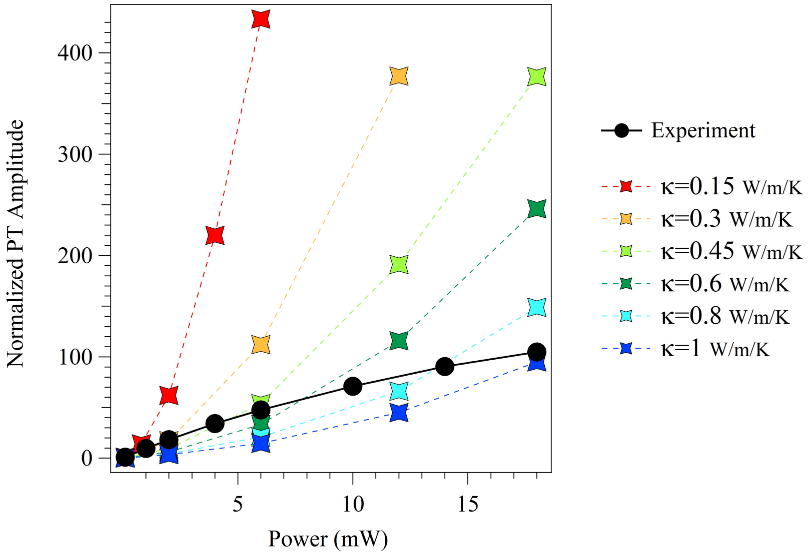

Figure 7: PT amplitude vs. heating power from experiment and from numerical simulations assuming a range of thermal conductivities for PDMS. (PT data are relative to 50 μW values.)

At this point to make further progress in the understanding of the observed PDMS behavior, a complementary method to probe the material changes in the vicinity of the NP would be desirable. Notwithstanding the absence of such a method for the time being, we take a step further and note that the dual amplitude phase measurement has the ability of constraining the simulations sufficiently to extract by a fitting procedure, the temperature dependence of the thermal parameters of the material surrounding the NP. To illustrate this point, Figure 8 shows the result of such fitting. The temperature dependence of conductivity was modeled with a 3-parameter power law (see Supporting Information - the "Temperature-dependent parameters of annealed PDMS" section). Adjusting conductivity alone could not fit both phase and amplitude data. This is because the phase characterizes retardation, i.e. depends on the heat diffusion velocity which is determined by diffusivity, not simply conductivity. Thus, it was necessary to model the thermal diffusivity independently, which was accomplished with a second degree polynomial in ΔT.

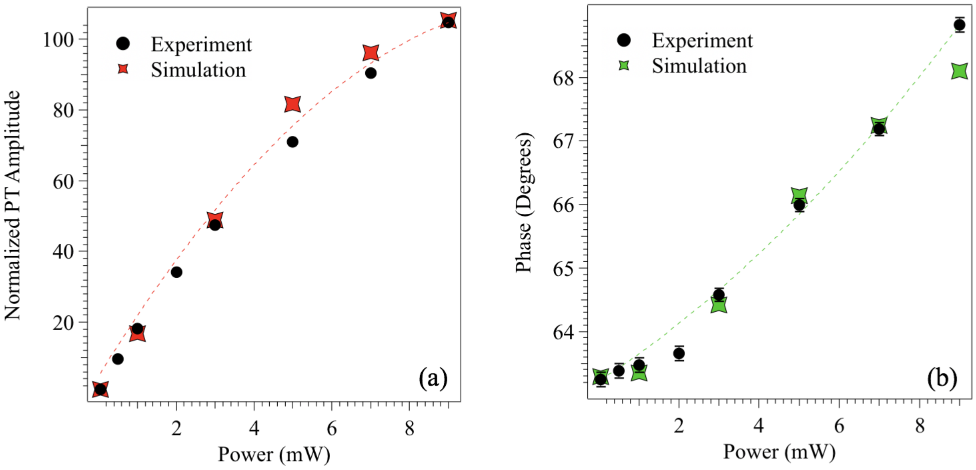

Figure 8: Experimental and numerically estimated PT amplitude (a) and phase (b) as a function of heating power, including $\alpha(T)$ and $\kappa(T)$.

Conclusion

In conclusion, the combined measurement and analysis of phase and amplitude in time-harmonic photothermal microscopy can open new avenues in the study of non-equilibrium phases obtained by nanoparticle-assisted photoannealing. We have demonstrated the detection of such a phase in PDMS and we discussed modalities of obtaining detailed material parameters information via comparisons with numerical simulations.

Methods

Optical

The PT imaging apparatus was described in ref.[19] However, for this work, refractive objectives were used since the wavelength was fixed and to maximize the maximum available power. The spatially-filtered pump and probe beams were focused at the sample by an objective lens with $\mathrm{NA}_{ill} = 1.4$ (Figure SI-1, and the PT power was detected by a fiber coupled Si pin photodiode with a collection objective of $\mathrm{NA}_{det} = 0.1$.

Gold NP Synthesis

Spherical, Au NPs from diameter 20 nm to 125 nm were synthesized. The NPs were coated with poly(dimethyl-diallyl-ammonium chloride) polymer (poly-DADMAC) (Mw=400000-500000, 20 $wt\%$ in water). All glassware was routinely cleaned with aqua regia and procedures carried out using Milli-Q water.

Au NPs are polyol synthesized first into nano-octahedra as reported.[55] A 0.4 mL portion of poly (DADMAC) was mixed with sodium hydroxide and ethylene glycol up to a total volume of 20 mL. The mixture was stirred at room temperature for 2 minutes. 0.5 M gold chloride was then added to the mixture and vigorously stirred for 15 minutes, or until all gold chloride had dissolved. This mixture was placed in a 195 $°C$ oil bath for 30 minutes. The reaction was performed under a condenser and then cooled to room temperature. The nano-octahedra edge length can be adjusted with the addition of basic conditions. The edges and vertices are then chemically etched as reported,[55] by the addition of 5 μL of 0.5 M gold chloride, resulting in highly spherical Au NPs. The Au NP diameter and morphology was measured using a JEOL JEM 1010 transmission electron microscope operating at 80 kV. The samples were prepared using diluted Au NP solutions pipetted onto carbon-coated copper grids and allowed to evaporate at room air. Diameter measurements were performed with the ImageJ software. Only samples of size distribution less than 10% were selected for the experiment. The concentration of each sample was measured using UV-VIS spectrometry at the plasmon resonance.

Immobilizing Gold NPs in PDMS

Approximately 200 μL solution of Au NPs prepared in "Gold NP Synthesis" section with $\sim 10^9 - 10^{10}\mathrm{mL}^{-1}$ concentration was incubated on a plasma discharged 1 : 10 poly-dimethyl siloxane layer ($\sim$ 100 micron thick) on a silica glass coverslip for 20 minutes. The PDMS layer was prepared by spin coating onto the silica substrate at 1200 rpm/min for 2 minutes. One droplet of 1 : 10 PDMS was added on top of the Au NP spread, covered by a second coverslip, and cured as per PDMS datasheet instructions.

Binding of Gold NPs to the Glass Substrate

Glass coverslips were sonicated with Milli-Q water 3 times and each time for 30 minutes. The sonicated glass coverslips were dried out with propane torch to remove the remaining residue from washing. The coverslip holder was then filled with methanol and 5% acetic acid. 500 μL of carboxyl ethyltrimethoxysilane was added to the solution. After 1.5 hours, the solution was removed and washed with Milli-Q water once. 100 μL of Au NP solution with a concentration of $\sim 10^{10}\ mL^{-1}$ was deposited on the glass coverslips and spin-coated with 2000 rpm/min after 30 minutes. A spacer to form a 1 mm thick chamber was placed, Milli-Q water was added, and the sample was covered with a second glass coverslip.

Acknowledgement

This work was supported by the U.S. Army Research Office: award number W911NF-20-1-0072, and the National Science Foundation: award number CHE - 1808027.

Supporting Information Available

The supplemental information document includes experimental setup schematics, discussions of experimental uncertainties, of the dependence of amplitude and phase on the frequency of modulation, of the spatial stability of the PT signal, of the simulation formalism as well as data comparing experiment and simulations of PT detected power in water. This material is available free of charge via the Internet at `http://pubs.acs.org/`.

References

1. Petrova, H.; Hu, M.; Hartland, G. V. Photothermal Properties of Gold Nanoparticles. *Zeitschrift für Phys. Chemie* **2007**, *221*, 361–376.

2. Huang, X.; El-Sayed, M. A. Gold nanoparticles: Optical properties and implementations in cancer diagnosis and photothermal therapy. *J. Adv. Res.* **2010**, *1*, 13–28.

3. Qin, Z.; Bischof, J. C. Thermophysical and biological responses of gold nanoparticle laser heating. *Chemical Society Reviews* **2012**, *41*, 1191–1217.

4. Kong, X.-T.; Khosravi Khorashad, L.; Wang, Z.; Govorov, A. O. Photothermal Circular Dichroism Induced by Plasmon Resonances in Chiral Metamaterial Absorbers and Bolometers. *Nano Lett.* **2018**, acs.nanolett.7b05446.

5. Govorov, A. O.; Richardson, H. H. Generating heat with metal nanoparticles. *Nano Today* **2007**, *2*, 30–38.

6. Berciaud, S.; Lasne, D.; Blab, G. A.; Cognet, L.; Lounis, B. Photothermal heterodyne imaging of individual metallic nanoparticles: Theory versus experiment. *Physical Review B* **2006**, *73*, 045424.

7. Vermeulen, P.; Cognet, L.; Lounis, B. Photothermal microscopy: optical detection of small absorbers in scattering environments. *J. Microsc.* **2014**, *254*, 115–121.

8. Li, Z.; Mao, W.; Devadas, M. S.; Hartland, G. V. Absorption spectroscopy of single optically trapped gold nanorods. *Nano letters* **2015**, *15*, 7731–7735.

9. Yorulmaz, M.; Nizzero, S.; Hoggard, A.; Wang, L.-Y.; Cai, Y.-Y.; Su, M.-N.; Chang, W.-S.; Link, S. Single-particle absorption spectroscopy by photothermal contrast. *Nano letters* **2015**, *15*, 3041–3047.

10. Joplin, A.; Chang, W.-S.; Link, S. Imaging and Spectroscopy of Single Metal Nanostructure Absorption. *Langmuir* **2018**, *34*, 3775–3786.

11. Tinglian, Y.; Yingyan, J.; Wei, W. Photothermal Microscopy: An Absorption-Based Single Molecule Imaging Technology. *PROGRESS IN CHEMISTRY* **2016**, *28*, 607–616.

12. Zharov, V.; Lapotko, D. Photothermal sensing of nanoscale targets. *Rev. Sci. Instrum.* **2003**, *74*, 785–788.

13. Selmke, M.; Braun, M.; Cichos, F. Photothermal single-particle microscopy: detection of a nanolens. *Acs Nano* **2012**, *6*, 2741–2749.

14. Zhang, Z.; Zhao, P.; Lin, P.; Sun, F. Thermo-optic coefficients of polymers for optical waveguide applications. *Polymer* **2006**, *47*, 4893–4896.

15. Berciaud, S.; Cognet, L.; Blab, G. A.; Lounis, B. Photothermal heterodyne imaging of individual nonfluorescent nanoclusters and nanocrystals. *Physical Review Letters* **2004**, *93*, 257402.

16. Boyer, D.; Tamarat, P.; Maali, A.; Lounis, B.; Orrit, M. Photothermal imaging of nanometer-sized metal particles among scatterers. *Science* **2002**, *297*, 1160–1163.

17. Van Dijk, M. A.; Lippitz, M.; Orrit, M. Far-field optical microscopy of single metal nanoparticles. *Accounts of chemical research* **2005**, *38*, 594–601.

18. van Dijk, M.; Tchebotareva, A.; Orrit, M.; Lippitz, M.; Berciaud, S.; Lasne, D.; Cognet, L.; Lounis, B. Absorption and scattering microscopy of single metal nanoparticles. *Physical Chemistry Chemical Physics* **2006**, *8*, 3486–3495.

19. Zahedian, M.; Koh, E. S.; Dragnea, B. Photothermal microspectroscopy with Bessel–Gauss beams and reflective objectives. *Applied Optics* **2019**, *58*, 7352–7358.

20. Heber, A.; Selmke, M.; Cichos, F. Thermal diffusivity measured using a single plasmonic nanoparticle. *Physical Chemistry Chemical Physics* **2015**, *17*, 20868–20872.

21. Heber, A.; Selmke, M.; Cichos, F. Thermal Diffusivities Studied by Single-Particle Photothermal Deflection Microscopy. *ACS Photonics* **2017**, *4*, 681–687.

22. Großer, J.; Furstenberg, R.; Kendziora, C. A.; Papantonakis, M. R.; Borchert, J.; Andrew McGill, R. Modeling of the heat transfer in laser-heated small particles on surfaces. *Int. J. Heat Mass Transf.* **2012**, *55*, 8038–8050.

23. Baffou, G.; Rigneault, H. Femtosecond-pulsed optical heating of gold nanoparticles. *Phys. Rev. B* **2011**, *84*, 035415.

24. Pavlovetc, I. M.; Podshivaylov, E. A.; Chatterjee, R.; Hartland, G. V.; Frantsuzov, P. A.; Kuno, M. Infrared photothermal heterodyne imaging: Contrast mechanism and detection limits. *J. Appl. Phys.* **2020**, *127*, 165101.

25. Pustovalov, V. K.; Smetannikov, A. S.; Zharov, V. P. Photothermal and accompanied phenomena of selective nanophotothermolysis with gold nanoparticles and laser pulses. *Laser Phys. Lett.* **2008**, *5*, 775–792.

26. Richardson, H. H.; Hickman, Z. N.; Govorov, A. O.; Thomas, A. C.; Zhang, W.; Kordesch, M. E. Thermooptical Properties of Gold Nanoparticles Embedded in Ice: Characterization of Heat Generation and Melting. *Nano Lett.* **2006**, *6*, 783–788.

27. Tijunelyte, I.; Guenin, E.; Lidgi-Guigui, N.; Colas, F.; Ibrahim, J.; Toury, T.; Lamy de la Chapelle, M. Nanoplasmonics tuned âĂIJclick chemistryâĂİ. *Nanoscale* **2016**, *8*, 7105–7112.

28. Carlson, M. T.; Green, A. J.; Richardson, H. H. Superheating Water by CW Excitation of Gold Nanodots. *Nano Lett.* **2012**, *12*, 1534–1537.

29. Baffou, G.; Polleux, J.; Rigneault, H.; Monneret, S. Super-heating and micro-bubble generation around plasmonic nanoparticles under cw illumination. *The Journal of Physical Chemistry C* **2014**, *118*, 4890–4898.

30. Li, X.; Wang, Y.; Zaytsev, M. E.; Lajoinie, G.; Le The, H.; Bomer, J. G.; Eijkel, J. C.; Zandvliet, H. J.; Zhang, X.; Lohse, D. Plasmonic Bubble Nucleation and Growth in Water: Effect of Dissolved Air. *J. Phys. Chem. C* **2019**, *123*, 23586–23593.

31. Li, M.; Lohmüller, T.; Feldmann, J. Optical Injection of Gold Nanoparticles into Living Cells. *Nano Lett.* **2015**, *15*, 770–775.

32. Hou, L.; Yorulmaz, M.; Verhart, N. R.; Orrit, M. Explosive formation and dynamics of vapor nanobubbles around a continuously heated gold nanosphere. *New J. Phys.* **2015**, *17*, 013050.

33. Wang, Y.; Zaytsev, M. E.; The, H. L.; Eijkel, J. C.; Zandvliet, H. J.; Zhang, X.; Lohse, D. Vapor and Gas-Bubble Growth Dynamics around Laser-Irradiated, Water-Immersed Plasmonic Nanoparticles. *ACS Nano* **2017**, *11*, 2045–2051.

34. Jones, S.; Andrén, D.; Antosiewicz, T. J.; Käll, M. Ultrafast Modulation of Thermoplasmonic Nanobubbles in Water. *Nano Lett.* **2019**, *19*, 8294–8302.

35. Xia, Y.; Whitesides, G. M. Soft Lithography. *Annual Review of Materials Science* **1998**, *28*, 153–184.

36. McDonald, J. C.; Duffy, D. C.; Anderson, J. R.; Chiu, D. T.; Wu, H.; Schueller, O. J.; Whitesides, G. M. Fabrication of microfluidic systems in poly (dimethylsiloxane). *ELECTROPHORESIS: An International Journal* **2000**, *21*, 27–40.

37. Fujii, T. PDMS-based microfluidic devices for biomedical applications. *Microelectronic Engineering* **2002**, *61*, 907–914.

38. Camino, G.; Lomakin, S.; Lazzari, M. Polydimethylsiloxane thermal degradation Part 1. Kinetic aspects. *Polymer* **2001**, *42*, 2395–2402.

39. Camino, G.; Lomakin, S.; Lageard, M. Thermal polydimethylsiloxane degradation. Part 2. The degradation mechanisms. *Polymer* **2002**, *43*, 2011–2015.

40. Luo, T.; Esfarjani, K.; Shiomi, J.; Henry, A.; Chen, G. Molecular dynamics simulation of thermal energy transport in polydimethylsiloxane. *Journal of applied physics* **2011**, *109*, 074321.

41. Yi, P.; Awang, R. A.; Rowe, W. S.; Kalantar-zadeh, K.; Khoshmanesh, K. PDMS nanocomposites for heat transfer enhancement in microfluidic platforms. *Lab on a Chip* **2014**, *14*, 3419–3426.

42. Gaiduk, A.; Ruijgrok, P. V.; Yorulmaz, M.; Orrit, M. Detection limits in photothermal microscopy. *Chemical Science* **2010**, *1*, 343–350.

43. Kuo, A. C. Polymer data handbook. *Polymer Data Handbook* **1999**,

44. Coker, A. K. *Fortran programs for chemical process design, analysis, and simulation*; Elsevier, 1995.

45. Kennedy, G.; Wasserburg, G.; Heard, H.; Newton, R. The upper three-phase region in the system SiO 2-H 2 O. *American Journal of Science* **1962**, *260*, 501–521.

46. Berto, P.; Mohamed, M. S.; Rigneault, H.; Baffou, G. Time-harmonic optical heating of plasmonic nanoparticles. *Physical Review B* **2014**, *90*, 035439.

47. Roberts, A. T.; Yang, J.; Reish, M. E.; Alabastri, A.; Halas, N. J.; Nordlander, P.; Everitt, H. O. Plasmonic nanoparticle-based epoxy photocuring: A deeper look. *Materials Today* **2019**, *27*, 14–20.

48. Dorsey, N. E. *Properties of Ordinary Water-substance in All Its Phases: Water-vapor, Water, and Ice*; Reinhold Publishing Corporation: Scranton, PA, 1940.

49. Tanaka, M.; Girard, G.; Davis, R.; Peuto, A.; Bignell, N. Recommended table for the density of water between 0 C and 40 C based on recent experimental reports. *Metrologia* **2001**, *38*, 301.

50. Struzziero, G.; Remy, B.; Skordos, A. A. Measurement of thermal conductivity of epoxy resins during cure. *J. Appl. Polym. Sci.* **2019**, *136*, 47015.

51. Setoura, K.; Ito, S.; Miyasaka, H. Stationary bubble formation and Marangoni convection induced by CW laser heating of a single gold nanoparticle. *Nanoscale* **2017**, *9*, 719–730.

52. Plech, A.; Cerna, R.; Kotaidis, V.; Hudert, F.; Bartels, A.; Dekorsy, T. A surface phase transition of supported gold nanoparticles. *Nano letters* **2007**, *7*, 1026–1031.

53. Dugdale, J. S.; MacDonald, D. K. Lattice thermal conductivity. *Phys. Rev.* **1955**, *98*, 1751–1752.

54. Anderson, D. Thermal conductivity of polymers. *Chemical Reviews* **1966**, *66*, 677–690.

55. Li, C.; Shuford, K. L.; Chen, M.; Lee, E. J.; Cho, S. O. A facile polyol route to uniform gold octahedra with tailorable size and their optical properties. *ACS nano* **2008**, *2*, 1760–1769.

Graphical TOC Entry

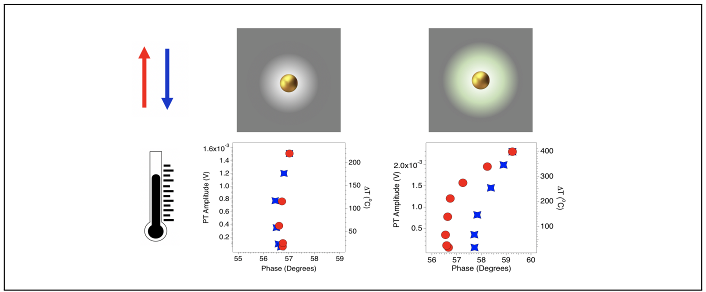

Nanoparticle-assisted photothermal annealing of PDMS to a denser phase occurs at temperatures above a threshold.